

Mid-infrared dielectric response of Fermi-degenerate electron-hole droplets in diamondJ. Omachi ^{1,2,3,*}, N. Naka ⁴, K. Yoshioka ^{2,3,5} and M. Kuwata-Gonokami ^{1,3,5,†}¹*Department of Applied Physics, School of Engineering, The University of Tokyo, Hongo, Bunkyo-ku, Tokyo 113-0033, Japan*²*Photon Science Center, School of Engineering, The University of Tokyo, Yayoi, Bunkyo-ku, Tokyo 113-8656, Japan*³*Core Research for Evolutional Science and Technology Agency, Kawaguchi-shi, Saitama 332-0012, Japan*⁴*Department of Physics, Kyoto University, Kitashirakawa, Sakyo-ku, Kyoto 606-8502, Japan*⁵*Department of Physics, School of Science, The University of Tokyo, Hongo, Bunkyo-ku, Tokyo 113-0033, Japan* (Received 11 July 2022; revised 17 November 2022; accepted 29 November 2022; published 15 December 2022)

Exploring the properties of a highly quantum-degenerate electron-hole (e-h) state as a many-body system is an interesting problem in solid-state physics. Electron-hole droplets (EHDs) offer a potential platform for investigating such a state of Fermi-degenerate carriers at an extremely high density. Herein we present dielectric response measurements of carriers in the mid-infrared (MIR) region for a definitive evaluation of the dynamic properties of the e-h state of EHDs in diamond. With photoexcitation across the band-gap energy by using the two-photon absorption process, we performed time-resolved differential transmission spectroscopy by using MIR probe light and time-resolved photoluminescence spectroscopy in the deep-ultraviolet region. By linking the two temporal profiles, we overcame the problem of previous ambiguous PL analyses and elucidated the MIR dielectric response that reveals the surface plasmon resonance (SPR) of EHDs and the effect of the e-h Coulomb interaction on the dynamic dielectric response. Thus, we found that the carrier density inside EHDs remained constant at $8 \times 10^{19} \text{ cm}^{-3}$ up to 2 ns, whereas a decay time of 1 ns of the condensed volume was found and the AC conductivity relaxation rate of $2 \times 10^{14} \text{ s}^{-1}$ maintained during this nanosecond timescale was the highest among group-IV semiconductors. We predicted a strong dependence of the e-h scattering rate on the probe frequency in the high-frequency region in which SPR appeared, suggesting that—when probed in the low-frequency region—dynamical relaxation does not interfere with the order formation expected in quantum-degenerate e-h systems at ultralow temperatures.

DOI: [10.1103/PhysRevB.106.235205](https://doi.org/10.1103/PhysRevB.106.235205)**I. INTRODUCTION**

Photoexcited semiconductors generate various electron-hole (e-h) states, depending on the carrier temperature and density. However, what kinds of states are exhibited when high-density e-h states are strongly quantum degenerate are still unclear. To explore such an unknown state, electron-hole droplets (EHDs) generated by spontaneous condensation from a lower-density exciton gas are attractive because they maintain a high-density state over nanoseconds [see Fig. 1(a)]. This study focuses on diamond as a potential platform for exploring a highly quantum-degenerate regime because the carrier density of EHDs is orders of magnitude higher than that among group-IV materials [1,2]. We attempt to quantitatively evaluate high-density carriers in EHDs by measuring the dynamic dielectric response in the mid-infrared (MIR) region.

EHDs have been found in three-dimensional indirect band-gap semiconductors, such as germanium (Ge), silicon (Si) [3], and diamond. In direct-band-gap materials without valley degeneracy of the conduction bands, such high-density states appear only when they are strongly

excited close to the Mott density [4]. Recent studies have shown that EHDs are formed at and above room temperature in quasi-two-dimensional monolayer transition metal dichalcogenides [5–7], which indicates that EHDs are useful for studying many-body interactions and device applications. EHDs are Fermi-degenerate states that vary in many aspects from other quantum-degenerate systems. Their unique elements include the Coulomb interaction, the mass imbalance between an electron and a hole, and the nonequilibrium nature of the system, all which are absent in superconductive electron gases in solids, Fermi atomic gases, and neutron stars. Therefore, the nucleation and decay dynamics of EHDs have attracted scientific attention for several years [3]. Historically, researchers have investigated EHDs mostly in Ge and Si in group-IV multivalley semiconductors by measuring the photoluminescence (PL) and induced absorption (IA) of far-infrared continuous-wave light from surface plasmon resonance (SPR) [3,8–10] and optical-pump terahertz-probe spectroscopy [11]. However, experimental observations have thus far been interpreted as analogous to water-drop condensation in a classical picture, and discussions remain qualitative within the relatively high-temperature range compared to a highly quantum-degenerate regime well below the Fermi temperature.

The existence of EHDs in diamond was discovered in 2000 in the PL spectra [1,2,12], which was made possible by deep-ultraviolet (DUV) laser technologies (necessary for

*Present address: School of Science, Kwansai Gakuin University, Gakuen-Uegahara, Sanda, Hyogo 669-1330, Japan.

†gonokami@phys.s.u-tokyo.ac.jp

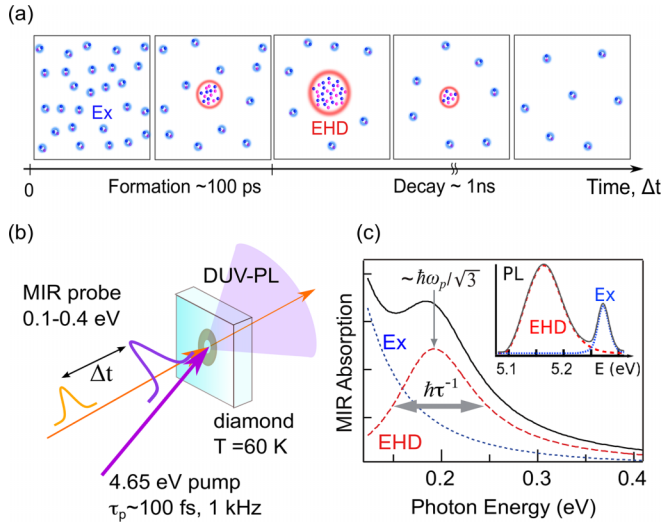


FIG. 1. (a) Schematic of the formation and decay dynamics of EHDs in diamond. (b) Experimental setup of deep-ultraviolet (DUV) pump–mid-infrared (MIR) probe spectroscopy combined with DUV photoluminescence (PL) spectroscopy. (c) Calculated MIR absorption spectrum of excitonic (Ex) internal transitions and surface plasmon resonance of EHDs in diamond. ω_p is the plasma frequency; τ^{-1} is the AC conductivity relaxation rate, where we assume τ^{-1} is frequency independent. Inset: Schematic of the DUV-PL spectrum in diamond.

carrier generation in diamond). Following the conventional method for Ge and Si, they fitted the PL spectrum of EHDs as a function of carrier density and temperature by the product of the density of states and the Fermi-Dirac distribution function. The linewidth and energy position of the emission spectrum provided clues for determining these two parameters. Conventional spectral analysis [1,2] has indicated a critical temperature T_c of the order of 100 K, as well as an extremely high carrier density n_D inside the EHDs, as shown in Table I. Furthermore, the high Fermi temperature T_F of approximately 680 K leads to the relation $T/T_F \ll 1$ at cryogenic temperatures (see Table I) and makes diamond a host of particular interest for highly quantum-degenerate e-h systems.

However, PL analysis includes ambiguities in the evaluation of density and temperature in the case of diamond. This is because of ambiguity in the inclusion of finite-size effects [13]

TABLE I. Comparison of material and carrier parameters in diamond, silicon, and germanium. Dielectric constant (ϵ_b), carrier density inside an EHD at $T = 0$ K ($n_{D,0K}$) (theoretical value) [2], critical temperature of EHD formation (T_c) [2], Fermi energy (E_F), Fermi temperature (T_F) [14], and T/T_F at $T = 2$ K in diamond, silicon, and germanium.

	Diamond	Si	Ge
ϵ_b	5.7	11.4	16.0
$n_{D,0K}$ (cm^{-3})	1.0×10^{20}	3.3×10^{18}	2.5×10^{17}
T_c (K)	165	24.5	6.7
T_F (K) [E_F (meV)]	680 (59)	130 (11)	35 (3.0)
T/T_F ($T = 2$ K)	0.003	0.02	0.06

in the theoretical curve of the PL spectrum when the droplet size is limited by the fast decay of the carriers unique to diamond [~ 1 ns, as sketched in Fig. 1(a)] [2]. For emission from a finite-size droplet, the spectral shape changes, and the energy position is blueshifted [15], making it difficult to determine the density and temperature accurately. In addition, the theoretical spectral shape cannot precisely consider carrier correlation effects; hence, the analysis is model dependent and an indirect evaluation method. Therefore, decisively extracting the time variation in the parameters that characterize the droplet remains challenging.

Here we address this issue by demonstrating that the densities, volume occupancies, and dynamical carrier scattering can be unambiguously evaluated by combining DUV pump–MIR probe spectroscopy with time-resolved DUV-PL spectroscopy, as shown in Fig. 1(b). We show that the dielectric response of EHDs and the photoionizing transition of excitons overlap spectrally in the MIR region. Our unique analysis, in contrast to other reports of DUV pump–MIR probe spectroscopy [16,17], enables us to extract the dielectric response of high-density carriers in EHDs. We extract the temporal profiles of EHDs and excitons from the decay characteristics of EHDs and exciton signals of DUV-PL and use them to separate the time-resolved spectrum of EHD and exciton components mixed in the MIR differential transmission (DT) spectrum. These analysis procedures enable the extraction of temporal variations in the parameters of EHDs without ambiguity, leading to quantitative confirmation of the high-density e-h system in EHDs. Interestingly, the EHDs decay in 1 ns by decreasing the volume while maintaining a density as high as $8 \times 10^{19} \text{ cm}^{-3}$ for up to 2 ns.

As shown in Fig. 1(c), we observe SPR of EHDs in the MIR region with a broad width. From this broadening we calculate the conductivity relaxation rate of the electrons and holes in the EHD to be as large as $2 \times 10^{14} \text{ s}^{-1}$. If this rate is attributed to the thermal collision of carriers, the corresponding effective temperature is surprisingly high (800 K) compared with T_c . We theoretically discuss three processes of scattering because of droplet finite-size effects, electron-phonon scattering, and carrier-carrier scattering as the origin of the broadening and the effects on the carrier temperature evaluation. The high e-h density in the EHD suggests the possibility of observing unique quantum phenomena in highly quantum-degenerate e-h systems, such as the appearance of the e-h Bardeen-Cooper-Schrieffer (BCS) phase. The energy scale that characterizes these phenomena is in the region of the terahertz (THz) frequency. Therefore, studying the effects of dynamic relaxation at the THz frequency is important.

The rest of this paper is organized as follows. In Sec. II we explain the experimental scheme and setup. In Sec. III A we present our experimental results and analyze the MIR spectra to extract the carrier density, AC conductivity relaxation rate, and volume occupancy of EHDs. In Sec. III B we evaluate temporal variations in these parameters. The correlation between the carrier density and AC relaxation rate allows us to discuss the origin of the carrier conductivity relaxation by considering the many-body effect. We also calculate the probe energy dependence of the AC relaxation rate and discuss the possibility of observing the BCS gap in the Coulomb-correlated e-h pairs. Finally, Sec. IV presents our conclusions.

II. EXPERIMENT

EHDs can be regarded as small metallic spheres floating in an exciton gas, as shown in Fig. 1(a). The dielectric response of this system is described well by the Drude response with SPR under the effective medium approximations [11,18] when the probe wavelength is significantly longer than the size of the metallic spheres. Based on the classical droplet formation model, the droplet size in diamond is expected to be a few hundred nanometers [19,20]. Therefore, this approximation is valid for time-resolved DT spectroscopy in the MIR region (MIR-DTS).

Following the Drude free-electron model, the dielectric function of e-h plasma as a metallic state is described by

$$\epsilon_M(\omega) = \epsilon_b(\omega) - \frac{\omega_p^2}{\omega(\omega + i\tau^{-1})}, \quad (1)$$

where ω is the optical frequency and $\epsilon_b(\omega) = [n(\omega) + i\kappa(\omega)]^2$ is the background dielectric function without photoexcitation. We assumed a refractive index $n(\omega)$ as determined by a Herzberger-type dispersion formula known for diamond [21]. In the MIR region, intrinsic absorption occurs with the creation of two and three phonons [22]. Thus, we deduced the extinction coefficient $\kappa(\omega) = \alpha_i(\omega)c/(2\omega)$ based on the intrinsic absorption coefficient $\alpha_i(\omega)$, measured in our sample at 60 K, by using a Fourier transform (FT) IR spectrometer and considering the reflections at the sample surfaces, where c is the speed of light. In Eq. (1),

$$\omega_p = \sqrt{\frac{n_D e^2}{\epsilon_0 \mu}} \quad (2)$$

is the plasma frequency with n_D as the carrier density, $\mu = 0.19 m_0$ (m_0 is the free-electron mass) as the reduced mass for an e-h pair, and ϵ_0 as the vacuum permittivity. τ^{-1} denotes the AC conductivity relaxation rate. Here, we assumed that the relaxation rate was equal for electrons and holes and that it was frequency independent. Based on the Maxwell-Garnett theory, the absorption coefficient for EHDs is described by

$$\alpha_D(\omega) = \frac{\omega}{cn(\omega)} \text{Im} \left[\frac{3\epsilon_b(\omega)f_D[\epsilon_M(\omega) - \epsilon_b(\omega)]}{(1 - f_D)[\epsilon_M(\omega) - \epsilon_b(\omega)] + 3\epsilon_b(\omega)} \right], \quad (3)$$

where f_D is the volume occupancy of EHDs. $\epsilon_b(\omega) = \{n(\omega) + i[\alpha_i(\omega) + \alpha_{ex}(\omega)]c/(2\omega)\}^2$ is the complex background dielectric constant, including IA coefficient $\alpha_{ex}(\omega)$ because of excitonic ionization [see Eq. (6)].

The dashed line in Fig. 1(c) is the mid-infrared induced absorption (MIR-IA) spectrum $\alpha_D(\omega)$, calculated for $n_D = 10^{20} \text{ cm}^{-3}$. The linewidth corresponds to the AC conductivity relaxation rate. The peak energy was approximately $\hbar\omega_p/\sqrt{3} = 0.2 \text{ eV}$. To observe the entire spectrum of α_D , we used MIR light ranging from 0.1 to 0.4 eV. The dotted line indicates the exciton internal transition from the $1s$ -bound state to the ionized continuum state, which spectrally overlaps with the Drude response of the EHDs. In the spectral analysis of MIR-DTS we determined the time-dependent relative amplitudes of the exciton and EHD components by using the different temporal responses between the exciton and EHD

components appearing at separate energy positions in the time-resolved DUV-PL spectra, as the inset of Fig. 1(c) shows. Section III B provides further details.

For our sample, we used a type IIa single-crystal diamond with a 337- μm thickness, grown for noncommercial purpose by using a high-temperature high-pressure method [23]. A nitrogen concentration of less than 0.1 ppm was confirmed by UV absorption spectroscopy, a boron concentration of less than 0.05 ppm by PL spectroscopy, and dislocation-free by x-ray projection topography [24,25]. We mounted the sample on a continuous-flow cryostat (Oxford Instruments, Microstat) at 60 K. We used this relatively high lattice temperature because EHDs can be detected most clearly in the PL spectra without the formation of polyexcitons [26]; thus, it is best suited for demonstrating the validity of the present experimental technique. We used a Ti:sapphire regenerative amplifier (Coherent, Libra) as the light source, with its center wavelength at 800 nm, pulse duration at ~ 100 fs, and repetition rate at 1 kHz. We divided the output into two beams. One generated a third-harmonic pump beam by wavelength conversion through two beta-barium borate crystals. We injected the second into an optical parametric amplifier (Light Conversion, TOPAS) and used it to generate the MIR probe beam through the difference-frequency generation of the signal and idler light.

We excited the sample above the band gap (5.5 eV) by using two-photon absorption [27] at an incident photon energy of 4.65 eV to generate high-density e-h pairs. The defocused pump beam having effectively a Gaussian profile was incident on the sample. The spot diameter (full-width at half-maximum, FWHM) was $169 \pm 18 \mu\text{m}$ on the incident surface with a reduction by 1.3% at the back surface. Under two-photon excitation, the penetration depth depends on the excitation power, the two-photon absorption coefficient (β), and the pulse duration (τ_p). Therefore, we estimated β/τ_p to be $(1.1 \pm 0.1) \times 10^4 \text{ cm J}^{-1}$ by using pulse-energy-dependent transmission measurements [28]. Because we need two photons to create one e-h pair, the photogenerated carrier density should be half the excitation density, as defined in Eq. (2) of Ref. [27].

We aligned the probe beam by using a metal pinhole with an aperture diameter of 200 μm placed on the sample surface and confirmed the spatial overlapping between the probe and pump beams. By using a 25-cm monochromator, we dispersed the transmitted MIR light and detected it by either a nitrogen-cooled HgCdTe detector for the probe energy from 0.1 to 0.2 eV or a nitrogen-cooled InSb detector from 0.2 to 0.4 eV. The spectral resolution was determined by the 0.10–0.15 μm wavelength intervals set by the monochromator, and was 2 meV at 0.1 eV and 8 meV at 0.4 eV. For MIR-DTS we obtained DT signals between pump-on and pump-off $\Delta T/T = (T_{\text{on}} - T_{\text{off}})/T_{\text{off}}$, by taking the signal at every shot by using a boxcar integrator with a sample-and-hold circuit. Repeating this procedure for probe wavelengths from 3 μm (0.41 eV) to 10 μm (0.12 eV) yielded the MIR response.

By using this procedure, we obtained MIR-IA spectra. We obtained temporal profiles by scanning a mechanical delay stage from $\Delta t = -100$ ps to $\Delta t = 2380$ ps in 40 ps steps at a fixed probe wavelength. For the time-resolved PL measurement, we sent the signal in the forward direction to a streak camera system (Hamamatsu Photonics, C5094) placed at the

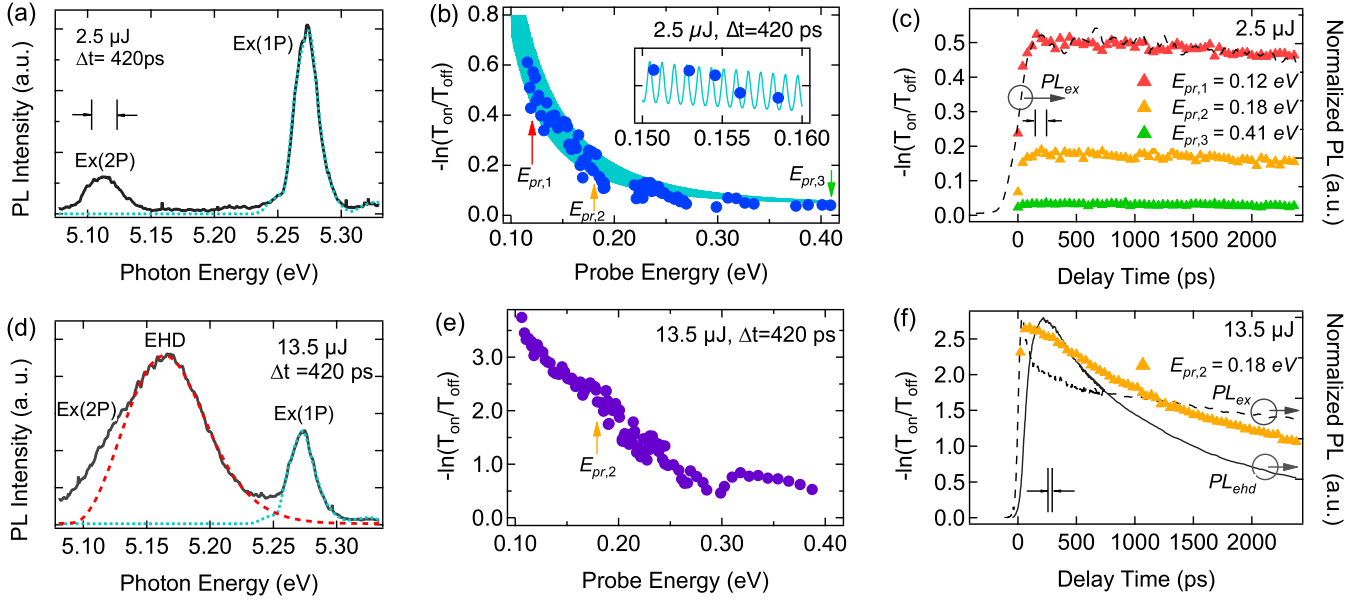


FIG. 2. (a) and (d) PL spectrum obtained at $\Delta t = 420$ ps. Black lines represent the data, whereas the cyan (dotted) and red (dashed) lines are fit functions for the exciton [Ex(1P)] and EHD components. All fit functions were convoluted with the spectral broadening function considering the finite slit width of the spectrometer. (b) and (e) MIR-IA spectrum at $\Delta t = 420$ ps. The cyan lines represent the MIR-IA spectra of excitons calculated by substituting α_{ex} given by Eq. (6) into α 's of Eq. (4), which includes the Fabry-Perot effect of the probe beam. (c) and (f) Temporal profiles of the MIR-IA and PL signals. We obtained (a) though (c) under low excitation ($2.5 \mu\text{J}$ pulse energy), while obtaining (d) through (f) under high excitation ($13.5 \mu\text{J}$ pulse energy). The temperature was set at 60 K.

exit slit of a 25-cm spectrometer. The spectral resolution was 0.020 eV in the DUV region.

III. RESULTS AND DISCUSSIONS

A. MIR-IA spectra and EHD parameters

First, we present the experimental results obtained by using weak excitation with a pulse energy of $2.5 \mu\text{J}$. We estimated the penetration length as 0.7 ± 0.1 mm and the corresponding excitation carrier density as $(8 \pm 2) \times 10^{15} \text{ cm}^{-3}$. Figure 2(a) shows the PL spectrum obtained at 420 ps after excitation. We observed one- and two-phonon-assisted emission lines from excitons [24], peaking at 5.27 and 5.12 eV, respectively [denoted as Ex(1P) and Ex(2P) in Fig. 2(a)]. By fitting a Maxwell-Boltzmann distribution function [12] to the emission lines from 5.233 to 5.330 eV considering contributions from four phonon modes and four fine-structure states of excitons [29,30] (see Appendix A), we obtained the effective excitonic temperature as $T_{\text{ex}} = 57.6 \pm 0.5$ K, which is in agreement with the set temperature of the cryostat.

The blue dots in Fig. 2(b) indicate the MIR-IA spectrum after a 420 ps delay. The data points appeared to scatter because of the Fabry-Perot effect of the probe beam in the sample; see the inset in Fig. 2(b). We obtained the cyan lines in Fig. 2(b) by calculating the quantity

$$-\ln\left(1 + \frac{\Delta T}{T}\right) = -\ln\left(\frac{\left|\frac{\tilde{r}_1 \tilde{r}_2 e^{i(\theta - \alpha d/2)}}{1 - \tilde{r}_1 \tilde{r}_2 e^{i(2\theta - \alpha d)}}\right|^2}{\left|\frac{\tilde{r}_1 \tilde{r}_2 e^{i\theta}}{1 - \tilde{r}_1 \tilde{r}_2 e^{i2\theta}}\right|^2}\right). \quad (4)$$

In this equation we included the pump-on effect in the complex phase difference. α is the coefficient of IA and d is

a parameter representing the effective interaction length between the probe and pump light, which depends on the excitation intensity. It takes the shorter one of the two values: the crystal thickness l or penetration length of the excitation pulse. $\theta = \tilde{n}l\omega/c$ is the phase difference without a pump, which is a function of the complex index of refraction $\tilde{n} = n + ik$. \tilde{r}_j ; \tilde{r}_j are the transmissions and reflections on the front ($j = 1$) and back ($j = 2$) sample surfaces, respectively.

Because the photon energy of the probe light was set higher than the binding energy of the exciton in diamond, we believe that the ($1s$) excitons in the ground state transitioned to the ionized state because of IA by the probe light. The coefficient of IA for excitons is expressed as

$$\alpha_{\text{ex}}(\omega) = \frac{\omega}{cn(\omega)d} \int_0^l dz \text{Im}[\chi_{\text{ex}}(z, \omega; \Gamma_{bb}, \Gamma_{bc})] \quad (5)$$

by using the susceptibility χ_{ex} based on the Lorentz oscillator model established for various excitonic systems [11,31–34], as presented in Appendix B. Here d is equal to the sample thickness l because the penetration depth is greater than l at this excitation level.

From Eq. (B1), $\chi_{\text{ex}}(z, \omega; \Gamma_{bb}, \Gamma_{bc})$ is proportional to the exciton density (n_{ex}) and is z dependent. Γ_{bb} and Γ_{bc} correspond to the damping rates of the exciton internal transitions from the $1s$ -bound state to higher-energy bound states (np) and from the $1s$ -bound state to the ionized continuum state, respectively. Here we rewrote $\text{Im}[\chi_{\text{ex}}(z, \omega; \Gamma_{bb}, \Gamma_{bc})] = \text{Im}[S(\omega; \Gamma_{bb}, \Gamma_{bc})]n_{\text{ex}}(z)$ for the explicit expression of the z dependence as follows:

$$\alpha_{\text{ex}}(\omega) = \frac{\omega}{cn(\omega)} \bar{n}_{\text{ex}} \text{Im}[S(\omega; \Gamma_{bb}, \Gamma_{bc})]. \quad (6)$$

In this equation, \bar{n}_{ex} is the excitonic density averaged over d , $\bar{n}_{\text{ex}} = \frac{1}{d} \int_0^d dz n_{\text{ex}}(z)$. We obtained a good agreement between the calculation and data after fitting by adjusting \bar{n}_{ex} in Eq. (6), while fixing the damping rates Γ_{bb} and Γ_{bc} to 0.001 eV. Consequently, we obtained an average excitonic density \bar{n}_{ex} of $8.7 \times 10^{15} \text{ cm}^{-3}$ after a 420 ps delay.

To confirm the origin of IA, we compared the temporal responses of MIR-IA at three probe energies (0.12, 0.18, and 0.41 eV) with that of the excitonic PL in the DUV region [dashed line in Fig. 2(c)]. We obtained the latter from a streak image cut along the temporal axis for excitons centered at 5.274 eV with a width of 0.045 eV. Based on the good agreement between these responses, we concluded that IA is indeed derived from excitons and that the amplitude reflects the number of excitons. After a 420 ps delay, the amount of IA decreased to 95% of its maximum value, as shown in Fig. 2(c). Because the initial carrier density was $(8 \pm 2) \times 10^{15} \text{ cm}^{-3}$, this result also verified the average excitonic density obtained by the spectral analysis explained previously.

Second, we studied DUV-PL and MIR-IA spectra under high excitation to explore the dielectric response of EHDs. Figure 2(d) shows the PL spectrum after a 420 ps delay with a pump pulse energy of 13.5 μJ , where we estimated the penetration depth to be $0.15 \pm 0.03 \text{ mm}$, which was shorter than the sample thickness. In addition to the Ex lines, a broad emission line peaking at 5.17 eV appeared because of one-phonon assisted PL from the EHDs [denoted as EHD in Fig. 2(d)] [1,2]. By fitting a Maxwell-Boltzmann distribution function to the emission lines from 5.256 to 5.333 eV, we obtained T_{ex} as $76.6 \pm 0.7 \text{ K}$. This temperature was higher than the set temperature of the cryostat sample holder. Such a temperature increase usually happens when excitons coexist with EHDs in diamond [27]. The heat source is explained by the phonons produced by the nonradiative Auger recombination process [35].

Figure 2(e) shows the simultaneously measured MIR-IA spectrum after a 420 ps delay. Compared to the spectrum under weak excitation, as shown in Fig. 2(b), we observed a bump structure at approximately 0.18 eV. This appeared to be induced by the response of EHDs, as expected in the previous section. Therefore, we considered that the time response of the MIR-IA signal was a mixture of these two components. By comparing it with the temporal profiles of PL, we indeed found that excitons and EHDs caused these two components. The triangles in Fig. 2(f) along the left axis represent the temporal response of IA at a probe energy of 0.18 eV as an example. The dashed and solid lines along the right axis show the temporal profiles of PL from excitons and EHDs, respectively. We obtained the latter from the streak image, which was cut along the temporal axis for droplets and integrated from 5.135 to 5.177 eV. We found that PL from the EHDs decayed exponentially with a time constant of approximately 1 ns, whereas that from excitons decayed more slowly. The response of MIR-IA differed from that of both excitons and EHDs. This situation differed from the case of weak excitation, as shown in Fig. 2(c).

To understand the MIR response under high excitation in more detail, Fig. 3(a) shows three representative temporal IA profiles with probe energies of 0.12, 0.2, and 0.4 eV, using triangles. We found that these profiles differed significantly.

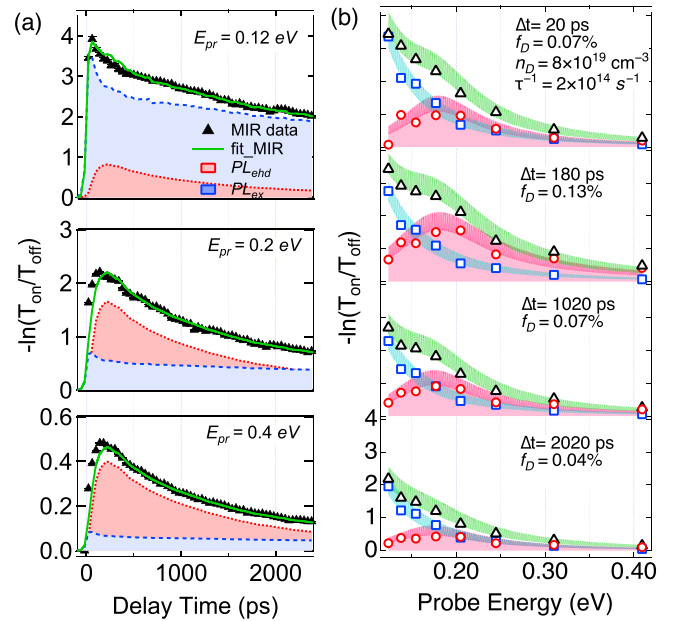


FIG. 3. (a) Temporal profiles of IA for a probe energy (E_{pr}) of 0.12, 0.2, and 0.4 eV (triangles), with a pump pulse energy of 13.5 μJ . The fitting curves obtained based on the temporal profiles of PL from EHDs (dotted line) and excitons (dashed line) are also shown. (b) Reconstructed MIR-IA spectrum after time delays of 20, 180, 1020, and 2020 ps (triangles). Circles and squares: Droplet and exciton components of the IA spectrum. Solid lines are their theoretical fits.

For a probe energy of 0.12 eV, the signal increased rapidly and decayed slowly, similar to the temporal profile of excitonic PL. In contrast, for probe energies of 0.2 and 0.4 eV, the signal increased slowly and decayed rapidly, similar to the temporal profile of droplet PL. These features indicate that MIR-IA includes contributions from both EHDs and excitons with different weights at different probe energies.

We reproduced the temporal profiles of MIR-IA at each probe energy—the triangles in Fig. 3(a)—as the weighted sum of the PL of excitons (dashed lines) and EHDs (dotted lines). By fitting the temporal range of 540 to 2380 ps, we obtained the weights. The solid line in each panel of Fig. 3(a) indicates the weighted sum. As shown in the two lower panels, the solid line slightly deviates from the triangles because the decomposition did not succeed earlier ($\Delta t \leq 180 \text{ ps}$), considered as an underestimation of the EHD contribution to the PL caused by the redshift of the spectrum immediately after excitation. Therefore, we extracted the EHD components from the spectrum—the red circles in Fig. 3(b)—by subtracting the exciton components (blue squares) from MIR-IA (triangles). The red lines on the circles represent the IA spectra of EHDs calculated according to α_D , as given by Eqs. (1)–(3). The peak energy remained almost constant, and only the amplitude decreased with time. We found consistency for the spectral shape of MIR-IA with the calculations performed by using the effective medium model, as schematically shown in Fig. 1(c). The cyan lines on the squares represent the IA induced by excitons. The green lines on the triangles represent the calculated sum of the EHD and exciton components.

The legends in Fig. 3(b) show the best-fit parameters n_D , f_D , and τ^{-1} for the four time delays. In this analysis we

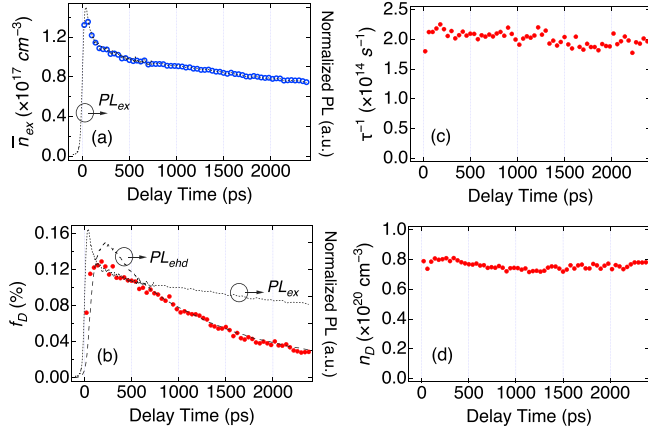


FIG. 4. Dynamics of (a) exciton density, (b) volume occupancy of EHDs, (c) AC conductivity relaxation rate in EHDs, and (d) density of e-h pairs in an EHD deduced from the analysis of MIR data at a pulse energy of 13.5 μJ and $T_{\text{set}} = 60$ K. (a) and (b) Dotted and dashed lines, respectively, for normalized temporal profiles of PL from excitons and EHDs.

assumed τ^{-1} in Eq. (1) was frequency independent. We found that n_{D} and τ^{-1} remained almost constant at approximately $8 \times 10^{19} \text{ cm}^{-3}$ and $2 \times 10^{14} \text{ s}^{-1}$ for all time delays. In contrast, f_{D} differed at time delays of 20, 180, 1020, 2020 ps, taking values of 0.07%, 0.13%, 0.07%, 0.04%, respectively.

After a time delay of 420 ps, the obtained value of n_{D} via MIR-IA analysis was $(7.6 \pm 0.6) \times 10^{19} \text{ cm}^{-3}$. For reference, we compare this with the case of a PL line-shape analysis. Compared to the methods in Refs. [1,2], the fitting function has been revised to include contributions of all four different phonon modes and to remove the uncertainties regarding the relative intensity ratio of these phonon modes (see Appendix A). By fitting with various initial parameters (n_{D} (5×10^{19} – $12 \times 10^{19} \text{ cm}^{-3}$), T (60–140 K), and E_{L} (5.205–5.245 eV)) to the emission lines from 5.140 to 5.233 eV, the evaluated values and errors for each parameter were $n_{\text{D}} = (7.5 \pm 0.4) \times 10^{19} \text{ cm}^{-3}$, $T = 126 \pm 4$ K, and $E_{\text{L}} = 5.232 \pm 0.002$ eV. The fitting curve is indicated by the dashed red line in Fig. 2(d). The obtained density value agreed with that obtained from the MIR-IA analysis within the error range. It should be kept in mind that the error of T is the accuracy in this fitting procedure and does not assert that the EHD temperature was determined with this accuracy.

B. Detailed dynamics of EHDs

After the fitting procedure discussed in the previous subsection, we deduced the temporal dynamics of \bar{n}_{ex} , f_{D} , τ^{-1} , and n_{D} . Figures 4(a)–4(d) show the results. The temporal dynamics of \bar{n}_{ex} —the circles in Fig. 4(a)—were the same as those of PL from excitons (dotted lines), indicating the consistency of this fitting procedure. f_{D} —dots in Fig. 4(b)—increased rapidly and reached a peak at 180 ps. Then, it decreased with the same dynamics as the PL from excitons (dotted line); lastly, at approximately 660 ps, its decay curve agreed with the exponential curve of PL from EHDs (dashed line). τ^{-1} remained almost constant with a value of

TABLE II. (Row 1) Reduced mass of an e-h pair in diamond, Si, and Ge [36], used in the numerical calculations of electron-phonon and e-h scattering. All masses are in units of the free-electron mass (m_0). (Rows 2–5) Carrier density, temperature, AC conductivity relaxation rate, and the rate obtained based on the FWHM of the IA spectrum from experiments in diamond (this study), Si [10], and Ge [8,9]. (Rows 6 and 7) Calculated rate because of electron-phonon scattering (τ_{ph}^{-1}) [37] and e-h scattering (τ_{eh}^{-1}) [38] (see text for details).

		Diamond	Si	Ge
	μ/m_0	0.19	0.12	0.047
Expt.	n_{D} (cm^{-3})	8×10^{19}	3.4×10^{18}	2.2×10^{17}
	T_{D} (K)	126	14	1.5
	τ^{-1} (s^{-1})	2×10^{14}	6×10^{12}	5×10^{12}
	FWHM/ \hbar (s^{-1})	2×10^{14}	2×10^{13}	1×10^{13}
Calc.	τ_{ph}^{-1} (s^{-1})	7×10^{10}	4×10^9	5×10^7
	τ_{eh}^{-1} (s^{-1})	9×10^{13}	1×10^{13}	3×10^{12}

$2 \times 10^{14} \text{ s}^{-1}$, as shown in Fig. 4(c), and n_{D} remained almost constant, with a value of $8 \times 10^{19} \text{ cm}^{-3}$, as shown in Fig. 4(d).

Based on these results, we unveiled the formation and decay dynamics of EHDs in diamond. The initial rapid increase in f_{D} and decrease in \bar{n}_{ex} indicate that the droplets grew by collecting excitons, as postulated in the classical droplet formation model. From 180 to 660 ps, when the temporal change of f_{D} was equivalent to that of \bar{n}_{ex} , the droplet size decreased by balancing the gain and loss rates of droplet growth, implying that the state was in quasiequilibrium. The loss rate consisted of exciton evaporation and carrier recombination [20]. Subsequently, the loss rate because of carrier recombination by the Auger process surmounted the gain rate as a result of the decrease in the surrounding exciton numbers. The almost constant value of n_{D} —even after f_{D} drops to 0.04% approximately at 2000 ps—indicates that the droplet maintains a constant e-h density after the formation of a stable liquid state as long as the surface energies are small.

The decay rate of f_{D} after 660 ps agreed well with the Auger recombination rate of $1/(Cn_{\text{D}}^2) = 1$ ns, where we used $C = 1 \times 10^{-31} \text{ cm}^6/\text{s}$ [2]. However, τ^{-1} was much higher than the Auger recombination rate, implying that the Auger process did not contribute to the relaxation of AC conductivity in the Drude response. We compared the AC conductivity relaxation rate in diamond with those in Ge [8,9] and Si [10] in Table II. Note that in Si and Ge, the rates were obtained by fitting the spectrally overlapping SPR and interband transitions between the light- and heavy-hole bands in the same energy region [9,10]. Therefore, the rates estimated from the FWHM of the IA spectra were larger than the conductivity relaxation rates for Si and Ge. In the case of diamond, interband transitions occurred in a frequency region significantly lower than the SPR frequency and did not affect the FWHM; therefore, an agreement occurred between the AC conductivity relaxation rate and the rate obtained based on the FWHM. The AC conductivity relaxation rate for diamond was the highest among the three materials. To investigate this origin, we discuss the scattering of high-density e-h systems with many-body interactions.

Generally, the conductivity relaxation processes reflected in the Drude response are derived from a change in carrier momentum. We considered three processes: momentum scattering because of the finite-size effect of a droplet, electron-phonon scattering, and carrier-carrier scattering.

In the first case, the rate is given by the Fermi velocity divided by the droplet radius R —that is, $1/R(\text{nm}) \times 10^{14} \text{ s}^{-1}$ at $n_D = 8 \times 10^{19} \text{ cm}^{-3}$. For example, when $R = 100 \text{ nm}$ [20], the rate was $1 \times 10^{12} \text{ s}^{-1}$. This value is significantly smaller than the estimated value. Additionally, the rate should increase when the droplet size decreases. Experimentally, τ^{-1} remains almost the same at $\Delta t \geq 180 \text{ ps}$, whereas the droplet size decreases, eliminating the possibility of this process. For the second case, Combescot and Bok discussed the rate by using the Boltzmann equation approach, including screening of the electron-phonon interaction by high-density carriers [37]. We considered only the interaction with longitudinal acoustic (LA) phonons [39] and used $m = m_{\text{oe}} = 0.39 m_0$ as the electron optical effective mass [36], $V_s = 1.8 \times 10^4 \text{ m/s}$ as the sound velocity, and $E_1 = 8.7 \text{ eV}$ as the deformation potential [40] in Eq. (30) of Ref. [37]. We obtained an electron-phonon scattering rate of $\tau_{\text{ph}}^{-1} = 7 \times 10^{10} \text{ s}^{-1}$, which is three orders of magnitude smaller than the experimental value. We also found that the calculated values of the electron-phonon scattering rate in Ge and Si (τ_{ph}^{-1} in Table II) were

$$\tau^{-1}(\omega_{\text{pr}}) = \frac{\hbar}{6n\mu\pi^3\omega_{\text{pr}}} \int_0^\infty d\omega \frac{\sinh\left(\frac{\hbar\omega_{\text{pr}}}{2k_B T}\right)}{\sinh\left(\frac{\hbar\omega_+}{2k_B T}\right)\sinh\left(\frac{\hbar\omega_-}{2k_B T}\right)} \times \int_0^\infty dq q^4 \text{Im}[\alpha(q, \omega_+)] \text{Im}[\alpha(q, \omega_-)] \left(\frac{1}{|4\pi\epsilon_0 + 2\alpha(q, \omega_+)|^2} + \frac{1}{|4\pi\epsilon_0 + 2\alpha(q, \omega_-)|^2} \right). \quad (7)$$

Here $\omega_{\pm} = \omega \pm \omega_{\text{pr}}/2$ and α is the polarizability defined in Ref. [38]. It has been reported that his theory effectively reproduces the MIR and terahertz response at room temperature [43] and a zero-frequency conductivity relaxation rate above 90 K in Si [44].

The open circles in Fig. 5 show the calculated relaxation rate because of e-h scattering as a function of probe energy ($E_{\text{pr}} = \hbar\omega_{\text{pr}}$). In our calculation we set $n = n_D$, $\mu = 0.19 m_0$, and $T = 126 \text{ K}$, which was a reference value obtained by PL line-shape analysis in the previous section. We found that the rate depended on the probe energy; it peaked at around 0.6–0.7 eV, which is ten times of the Fermi energy (E_F) and slightly higher than the probe energies (0.1–0.4 eV) of the MIR-DTS. The theoretical value was $9 \times 10^{13} \text{ s}^{-1}$ at the highest probe energy of 0.4 eV in our experiment, whereas it was $5 \times 10^{13} \text{ s}^{-1}$ at the lowest probe energy of 0.1 eV. These values were found to be from 2 to 5 times lower than the value obtained in our experiments (the red line in Fig. 5).

In Eq. (7) we ignored the nonparabolicity of the valence bands [45] and the anisotropy of the conduction and valence bands. If we considered the former effect, the number of final states of e-h scattering would increase because of the heavier effective masses at larger wave vectors. In the latter effect, new channels by electron-electron and hole-hole scat-

tering might open in multiple anisotropic bands, in addition to e-h scattering [42]. Thus, the actual relaxation rate can be higher than the calculated value by one order, as described in Ref. [42], and the ambiguity in these correction factors could explain the difference between the calculated and experimental values.

Similarly, we calculated the rate of e-h scattering for Si and Ge at the peak energy of the SPR of EHDs—that is, 0.034 [10] and 0.009 eV [8], respectively—as τ_{eh}^{-1} in Table II. The theoretical value of $1 \times 10^{13} \text{ s}^{-1}$ for Si resulted between the experimental values of τ^{-1} and the rate corresponding to the FWHM. For Ge, the theoretical value of $3 \times 10^{12} \text{ s}^{-1}$ is in close agreement with $\tau^{-1} = 5 \times 10^{12} \text{ s}^{-1}$. The highest relaxation rate found in diamond was consistent with the highest observed carrier density in a droplet among the three materials. Furthermore, the highest effective carrier temperature and lowest dielectric constant enhanced the rate. The number of carriers contributing to scattering increases with temperature, and attenuated Coulomb screening leads to an enhancement in the relaxation rate. The above discussion suggests that the large relaxation rate of the AC conductivity in diamond can be explained by the effect of the Coulomb interaction between electrons and holes on the dynamic dielectric response.

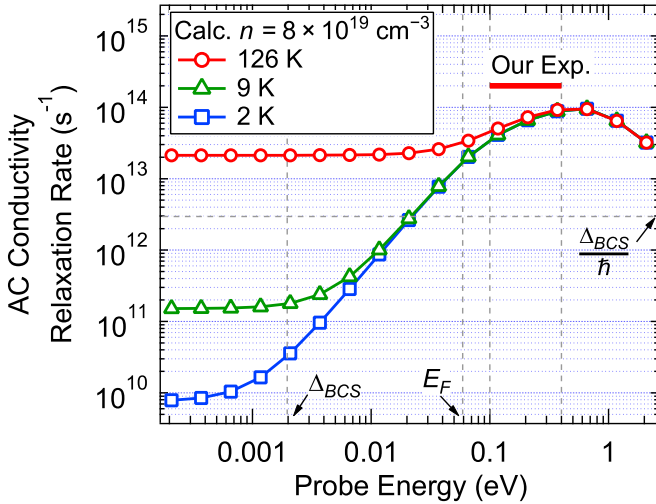


FIG. 5. Calculated relaxation rate because of e-h scattering at a carrier density of $8 \times 10^{19} \text{ cm}^{-3}$ in diamond at 126 K (open circles), 9 K (open triangles), and 2 K (open squares) versus the probe energy. Our experimental value estimated from MIR-IA at probe energies from 0.1 to 0.4 eV is shown by the solid line. Downward arrows denote the Fermi energy (E_F) and gap energy (Δ_{BCS}) of the e-h BCS state. The horizontal dashed line denotes the rate corresponding to the BCS gap energy.

Now that we have elucidated using the MIR dielectric response that a remarkably high-density e-h state exists in EHDs in diamond, we can discuss a future prospective investigation of the quantum-degenerate states expected at high densities and low temperatures. Based on the isotropic two-band model discussed by Mizoo *et al.* [46], when the carrier density is $8 \times 10^{19} \text{ cm}^{-3}$, the e-h BCS gap (Δ_{BCS}) is estimated to be 0.002 eV with an angular frequency of $\Delta_{\text{BCS}}/\hbar = 3 \text{ THz}$, with the critical temperature (T_c^{BCS}) at 9 K [47–49]. The Auger recombination process, which determines the population decay rate, does not prevent gap opening because the Auger rate (1 GHz) is three orders of magnitude lower than the gap frequency. Regarding the momentum decay rate, our estimation revealed that the AC conductivity relaxation rate considering e-h scattering is expected to be significantly lower than the gap frequency when the probe energy is set below the gap frequency, as indicated by the open triangles at 9 K and squares at 2 K in Fig. 5. The rate of relaxation by acoustic phonon scattering was predicted to be reduced to 8 MHz at T_c^{BCS} because of the quantum phase-space restriction [37]. However, when the droplet size was decreased to 100 nm, the size-dependent rate became equivalent to the gap frequency.

A future challenge is to lower the temperature of the high-density e-h system to observe the quantum-degenerate state. To achieve this, the temperature of the EHD must be evaluated unambiguously. In this study we evaluated the carrier temperatures based on PL line-shape analysis, which limits the quantitiveness of the obtained values. In the dynamic dielectric response, the linewidth of the dielectric response is expected to be independent of the carrier temperature in the MIR region based on the theoretical curves of the AC conductivity relaxation rate shown in Fig. 5. Therefore, an accurate temperature evaluation by using the linewidth of the

SPR spectrum is not expected. However, because the relaxation rate strongly depends on the carrier temperature in the low-frequency region, if the probe frequency is extended to the THz region and the induced complex dielectric response can be measured with high precision, the carrier temperature could be evaluated by spectral analysis. One possible way to lower the temperature of the EHD is to reduce the Auger recombination rate, which is proportional to the square of the carrier density and is believed to be responsible for the increase in the carrier temperature [50]. For example, if we applied strain in the [100] direction and reduced the valley degeneracy [51], the carrier density of the droplet would be reduced to 0.3 times the current density, which would reduce the Auger rate by one order of magnitude.

Finally, we give a brief comment on the sample dependence. Because the decay rate of carriers in EHDs is considered to be determined by the Auger recombination due to the e-h many-body interaction rather than impurity trapping, we believe that the AC conductivity relaxation and the decay dynamics of EHDs discussed for high-purity samples as used in this study are insensitive to the sample quality and can be treated as an intrinsic phenomenon. By contrast, we have observed that the ratio of the EHDs to exciton emission lines tends to be higher when the impurity concentration is higher, which indicates that the EHD formation may be triggered by impurity sites [24]. In addition, the emission from EHDs is observed up to higher temperatures for samples with fewer dislocations [25]. These results suggest that it would be interesting to investigate the impurity/dislocation dependence of the formation and the stability of EHDs.

IV. CONCLUSION

We characterized the e-h states of EHDs in diamond at 60 K by performing MIR-DTS in addition to time-resolved PL spectroscopy. We succeeded in separating the broadband MIR spectra into two components, one because of excitonic internal transitions and the other because of SPR of the EHDs. We applied the Maxwell-Garnett theory to the spectral analysis of SPR.

A unique feature of this analysis is that the carrier density of the EHD can be evaluated directly from the peak frequency of the SPR spectrum, and the dynamics of the density, volume occupancy of the EHD, and AC conduction relaxation rate can be evaluated. The carrier density was as high as $8 \times 10^{19} \text{ cm}^{-3}$ up to 2 ns. The relationship between the time evolution of exciton density and EHD volume occupancy revealed that the classical droplet formation model was effective in explaining the dynamics of EHD formation and decay in diamond.

The AC conductivity relaxation rate was found to be $2 \times 10^{14} \text{ s}^{-1}$ —the highest value among group IV semiconductors. Owing to the effect of the Coulomb interaction between electrons and holes in the dynamic dielectric response, the relaxation rate of the AC conductivity strongly depended on the probe frequency of the electromagnetic wave that drove the e-h motion. Theoretical calculations revealed that the relaxation rate will be highest at a frequency near the SPR resonance of the EHDs, and that the SPR linewidth will be dominated by temperature-insensitive e-h scattering. Conversely, the relaxation rate in a lower frequency region was

dependent on the carrier temperature and decreased with decreasing temperature. Therefore, the carrier temperature could be evaluated if the probe energies are extended to a lower frequency region in the THz range. Furthermore, capturing the BCS transition might be possible by suppressing e-h scattering, which may interfere with the macroscopic quantum phenomena in Fermi-degenerate e-h systems at low temperatures.

This study indicates that the EHD in diamond is in a remarkably dense e-h state. The temperature evaluation and generation of a low-temperature, high-density e-h state are challenges to be addressed in the future. If such a state can be realized, we could observe macroscopic e-h quantum states that have not been previously observed.

ACKNOWLEDGMENTS

We thank T. Suzuki, K. Kato, and T. L. Nguyen for supporting the experiments, and H. Sumiya (Sumitomo Electric Industries Ltd.) for providing the high-quality sample. We also thank Dr. Inagaki for calculating the transition temperature of the e-h BCS state and for helpful discussion. We thank Dr. Sakurai for critically reviewing this paper. This study was supported by the Grant-in-Aid for Scientific Research on Innovative Area ‘Optical science of dynamically correlated electrons (DYCE)’ No. 20104002, Photon Frontier Network Program, Project for Developing Innovation Systems, and Advanced Integration Science Innovation Education and Research Consortium Program of MEXT, Japan, JSPS KAKENHI (Grant Nos. JP20224006, JP26247049, JP26400317, JP21H04673, and JP22H01156), and JSPS through Funding Program for World-Leading Innovative R&D on Science and Technology (FIRST Program).

APPENDIX A: PL SPECTRAL ANALYSIS

To calculate the theoretical curve of one-phonon assisted PL from excitons, we considered the contributions from four different phonon modes, i.e., longitudinal optical (LO), transverse optical (TO), LA, and transverse acoustic (TA) phonons, and also fine-structure states of excitons. The relative intensity ratio of TO:LA:TA was set to be 1:0.06:0.07 based on theoretical values [30]. The relative ratio of LO:TO was determined to be 0.03:1 from fitting results of the exciton emission in Fig. 2(a), since the LO component of the exciton emission has little overlap in the spectrum with the TO component. The contributions from the four fine-structure states of excitons (EX l , $l = 1, 2, 3, 4$) was considered by the Boltzmann factor, which depends on the energy separations of the four components, and also the relative intensity ratio obtained by derivative of the absorption spectra in Ref. [30] and reported values in Ref. [29] (see Table III). The energy separations of EX2, EX3, and EX4 to EX1 were set to 3.6, 6.7, and 13.6 meV [29].

The theoretical curve of one-phonon assisted PL from EHDs is described by a convolution of the electron and hole density of states and Fermi-Dirac distribution function [52] considering contributions of four phonon modes,

which is

$$I_{\text{EHD}}(\omega; A, n_D, T, E_L) = A \sum_j a_j \int_0^\infty d\epsilon_e \sqrt{\epsilon_e} f(\epsilon_e - E_F^e, T) \sqrt{\epsilon_h} f(\epsilon_h - E_F^h, T) \times \delta(\hbar\omega - \epsilon_e - \epsilon_h - E_L + \hbar\Omega_j), \quad (\text{A1})$$

where A is a constant, a_j is the relative ratio for each phonon mode j with the phonon energy $\hbar\Omega_j$, $f(E, T) = [1 + \exp(-E/k_B T)]^{-1}$ is the Fermi-Dirac distribution function at the carrier temperature of T . E_F^e and E_F^h are the electron and hole Fermi energies at the carrier density n_D and carrier temperature T , which is $E_F^{e(h)} = \hbar^2(3\pi^2 n_D)^{2/3} / (2m_{de(dh)}) - (k_B T)^2 \pi^2 m_{de(dh)} / [6\hbar^2(3\pi^2 n_D)^{2/3}]$ with $m_{de} = 1.64m_0$ and $m_{dh} = 0.94m_0$ [36]. E_L represents the low-energy edge of the PL spectrum, which is conventionally taken as the renormalized gap and is a function of n_D and T ; however, because the energy edge is blueshifted for the PL of finite-size droplets [15], its effect must be included in E_L . Therefore, during optimization of the fitting function, we set A, n_D, T , and E_L as free parameters. We set the fitting range from 5.140 to 5.233 eV for the present line-shape analysis for EHDs, because below 5.14 eV, the emission lines of EHDs overlap with two-phonon-assisted emission lines of excitons [Ex(2P)].

APPENDIX B: OPTICAL SUSCEPTIBILITY DUE TO EXCITONIC INTERNAL TRANSITIONS

Based on the Lorentz oscillator model, the optical susceptibility because of excitonic internal transitions [31–33] is given by

$$\chi_{\text{ex}}(z, \omega; \Gamma_{bb}, \Gamma_{bc}) = n_{\text{ex}}(z) \frac{e^2}{\epsilon_0 \mu} \left(\sum_{n=0}^{\infty} \frac{f_{1s,np}}{\left(\frac{E_{np} - E_{1s}}{\hbar}\right)^2 - \omega^2 - i\omega\Gamma_{bb}} + \frac{L}{\pi} \int dk \frac{f_{1s}(k)}{\left(\frac{E(k) - E_{1s}}{\hbar}\right)^2 - \omega^2 - i\omega\Gamma_{bc}} \right), \quad (\text{B1})$$

where we consider spin degeneracy and use the following parameters: 1s-exciton energy $E_{1s} = -R_y$, np -exciton energy $E_{np} = -R_y/n^2$, and the kinetic energy for the ionized state $E(k) = \hbar^2 k^2 / 2\mu$. L is in units of length and is used to normalize the hydrogenlike wave function of the excitons [33], where $L \rightarrow \infty$. The first term in Eq. (B1) represents transitions from

TABLE III. Relative ratio of contributions from four phonon modes (a_j) and the excitonic fine structure for each phonon modes (EX1–EX4) [29,30].

j	a_j	EX1	EX2	EX3	EX4
LO	0.03	0.07	0.2	1	0.6
TO	1	0.03	1	0.6	0.9
LA	0.06	0.09	0.09	1	1.1
TA	0.07	0.04	1	0.4	0.8

the ground state ($1s$) exciton to higher-energy states (np), and the second term transitions from $1s$ to the ionized continuum. Γ_{bb} and Γ_{bc} correspond to the damping rates for each transition, considered as $\Gamma_{bb} = \Gamma_{bc} = 1$ meV. Then, the oscillator strengths for the transition from $1s$ to an np or continuum state

are given by

$$f_{1s,np} = \frac{2^{10} \mu a^2 (E_{np} - E_{1s})}{3\hbar^2} \frac{n^7}{(n+1)^{2n+5} (n-1)^{-2n+5}} \quad (\text{B2})$$

and

$$f_{1s}(k) = \frac{2^{10} \mu a^2 [E(k) - E_{1s}] \pi}{3\hbar^2} \frac{a^2 k \left(\frac{i+ak}{i-ak}\right)^{-\frac{2i}{ak}}}{L (1 + a^2 k^2)^5 (1 - e^{-\frac{2\pi}{ak}})}, \quad (\text{B3})$$

where $a = 1.5$ nm is the excitonic Bohr radius.

We assumed that the ground state of excitons has four levels because of fine-structure splitting [29]. For the thermal distribution we used the excitonic temperature deduced from the line-shape analysis of the PL spectrum.

-
- [1] K. Thonke, R. Schliesing, N. Teofilov, H. Zacharias, R. Sauer, A. M. Zaitsev, H. Kanda, and T. R. Anthony, *Diam. Relat. Mater.* **9**, 428 (2000).
- [2] R. Shimano, M. Nagai, K. Horiuchi, and M. Kuwata-Gonokami, *Phys. Rev. Lett.* **88**, 057404 (2002).
- [3] *Electron-Hole Droplets in Semiconductors*, edited by C. D. Jefferies and L. V. Keldysh (North-Holland, Amsterdam, 1983).
- [4] F. Sekiguchi, T. Mochizuki, C. Kim, H. Akiyama, L. N. Pfeiffer, K. W. West, and R. Shimano, *Phys. Rev. Lett.* **118**, 067401 (2017).
- [5] T. B. Arp, D. Pleskot, V. Aji, and N. M. Gabor, *Nat. Photonics* **13**, 245 (2019).
- [6] R. Younts, A. Bataller, H. Ardekani, Y. Yu, L. Cao, and K. Gundogdu, *Phys. Status Solidi B* **256**, 1900223 (2019).
- [7] R. L. Wilmington, H. Ardekani, A. Rustagi, A. Bataller, A. F. Kemper, R. A. Younts, and K. Gundogdu, *Phys. Rev. B* **103**, 075416 (2021).
- [8] V. S. Vavilov, V. A. Zayats, and V. N. Murzin, *Pis'ma Zh. Eksp. Teor. Fiz.* **10**, 304 (1969) [*JETP Lett.* **10**, 192 (1969)].
- [9] J. H. Rose, H. B. Shore, and T. M. Rice, *Phys. Rev. B* **17**, 752 (1978).
- [10] H. Navarro, H. G. Zarate, and T. Timsuk, *Solid State Commun.* **25**, 1045 (1978).
- [11] T. Suzuki and R. Shimano, *Phys. Rev. Lett.* **103**, 057401 (2009).
- [12] M. Nagai, R. Shimano, K. Horiuchi, and M. Kuwata-Gonokami, *Phys. Rev. B* **68**, 081202(R) (2003).
- [13] C. Benoit á la Guillaume, B. Etienne, and M. Voos, *Physics of Highly Excited States in Solids*, Lecture Notes in Physics (Springer, Berlin, 1976), Vol. 57, p. 177.
- [14] Here we define the Fermi energy as the average of that for the photogenerated electrons and holes. The Fermi temperature is given by $T_F = E_F/k_B$.
- [15] T. Tamaya, K. Kamide, and T. Ogawa, *J. Phys. Soc. Jpn.* **81**, SB060 (2012).
- [16] M. Kozák, F. Trojánek, T. Popelář, and P. Malý, *Diam. Relat. Mater.* **34**, 13 (2013).
- [17] T. Popelář, F. Trojánek, M. Kozák, and P. Malý, *Diam. Relat. Mater.* **71**, 13 (2017).
- [18] C. F. Bohren and D. R. Huffman, *Absorption and Scattering of Light by Small Particles* (Wiley, New York, 1983).
- [19] R. M. Westervelt, *Phys. Status Solidi B* **74**, 727 (1976).
- [20] J. H. Jiang, M. W. Wu, M. Nagai, and M. Kuwata-Gonokami, *Phys. Rev. B* **71**, 035215 (2005).
- [21] D. Edwards and H. R. Phillipp, Cubic carbon (diamond), in *Handbook of Optical Constants of Solids*, edited by E. D. Palik (Academic, Orlando, FL, 1985), p. 665.
- [22] C. Piccirillo, G. Davies, A. Mainwood, S. Scarle, C. M. Penchina, T. P. Mollat, K. L. Lewis, M. Nesládek, Z. Remes, and C. S. J. Pickles, *J. Appl. Phys.* **92**, 756 (2002).
- [23] H. Sumiya and S. Satoh, *Diam. Relat. Mater.* **5**, 1359 (1996).
- [24] N. Naka, J. Omachi, H. Sumiya, K. Tamasaku, T. Ishikawa, and M. Kuwata-Gonokami, *Phys. Rev. B* **80**, 035201 (2009).
- [25] K. Tamasaku (private communication).
- [26] J. Omachi, T. Suzuki, K. Kato, N. Naka, K. Yoshioka, and M. Kuwata-Gonokami, *Phys. Rev. Lett.* **111**, 026402 (2013).
- [27] N. Naka, T. Kitamura, J. Omachi, and M. Kuwata-Gonokami, *Phys. Status Solidi B* **245**, 2676 (2008).
- [28] S. Preuss and M. Stuke, *Appl. Phys. Lett.* **67**, 338 (1995).
- [29] Y. Hazama, N. Naka, and H. Stolz, *Phys. Rev. B* **90**, 045209 (2014).
- [30] K. Konishi and N. Naka, *Phys. Rev. B* **104**, 125204 (2021).
- [31] M. Shinada and S. Sugano, *J. Phys. Soc. Jpn.* **21**, 1936 (1966).
- [32] U. Ekenberg and M. Altarelli, *Phys. Rev. B* **35**, 7585 (1987).
- [33] H. Haug and S. W. Koch, *Quantum Theory of the Optical and Electronic Properties of Semiconductors* (World Scientific, Singapore, 2004).
- [34] R. A. Kaindl, D. Hagele, M. A. Carnahan, and D. S. Chemla, *Phys. Rev. B* **79**, 045320 (2009).
- [35] A. Haug, *Solid State Commun.* **25**, 477 (1978).
- [36] N. Naka, K. Fukai, Y. Handa, and I. Akimoto, *Phys. Rev. B* **88**, 035205 (2013).
- [37] M. Combescot and J. Bok, *Phys. Rev. B* **35**, 1181 (1987).
- [38] B. E. Sernelius, *Phys. Rev. B* **43**, 7136 (1991).
- [39] We do not consider scattering by longitudinal-optical (LO) phonons because the LO phonon energy is 160 meV in

- diamond, and the corresponding temperature is ~ 1860 K, which is one order of magnitude higher than the carrier temperature.
- [40] F. Nava, C. Canali, C. Jacoboni, L. Reggiani, and S. F. Kozlov, *Solid State Commun.* **33**, 475 (1980).
- [41] M. Combescot and R. Combescot, *Phys. Rev. B* **35**, 7986 (1987).
- [42] B. E. Sernelius, *Phys. Rev. B* **40**, 12438 (1989).
- [43] F. Meng, M. D. Thomson, B. E. Sernelius, M. Jörger, and H. G. Roskos, *Phys. Rev. B* **91**, 075201 (2015).
- [44] T. Terashige, H. Yada, Y. Matsui, T. Miyamoto, N. Kida, and H. Okamoto, *Phys. Rev. B* **91**, 241201(R) (2015).
- [45] C. Jacoboni and L. Reggiani, *Rev. Mod. Phys.* **55**, 645 (1983).
- [46] K. Mizoo, T. J. Inagaki, Y. Ueshima, and M. Aihara, *J. Phys. Soc. Jpn.* **74**, 1745 (2005).
- [47] T. J. Inagaki and M. Aihara, *Phys. Rev. B* **66**, 075204 (2002).
- [48] T. J. Inagaki (private communication).
- [49] The values of the e-h BCS gap and critical temperature depend on the binding energy of the exciton. For this evaluation we used a binding energy of 0.080 eV. Considering exciton fine-structure splitting, excitons occupy the lowest level at ultralow temperatures after thermal equilibrium, and their binding energy is 0.094 eV [53]. When the binding energy was 0.094 eV, the e-h BCS gap and critical temperature were estimated as 0.006 eV and 18 K, respectively. For probe energies below the gap, the AC conductivity rate is lower than the gap frequency.
- [50] Y. Hazama, N. Naka, M. Kuwata-Gonokami, and K. Tanaka, *Europhys. Lett.* **104**, 47012 (2013).
- [51] N. Naka, J. Omachi, and M. Kuwata-Gonokami, *Phys. Rev. B* **76**, 193202 (2007).
- [52] T. K. Lo, *Solid State Commun.* **15**, 1231 (1974).
- [53] T. Ichii, Y. Hazama, N. Naka, and K. Tanaka, *Appl. Phys. Lett.* **116**, 231102 (2020).